

# A MEMS Nanopositioner With Integrated Tip for Scanning Tunneling Microscopy

Afshin Alipour<sup>1</sup>, M. Bulut Coskun<sup>2</sup>, and S. O. Reza Moheimani<sup>3</sup>, *Fellow, IEEE*

**Abstract**—Slow Z-axis dynamics of Scanning Tunneling Microscope (STM) is a key contributing factor to the slow scan speed of this instrument. A great majority of STM systems use piezotube nanopositioners for scanning. The piezotube bulkiness along with the mass of STM tip assembly restrict the overall Z-axis bandwidth of the system to about  $1\text{ kHz}$ . This limited bandwidth slows down the STM response to the sample topography changes. In this paper, we report a microfabrication process to build a Microelectromechanical-System (MEMS) nanopositioner for Z-axis positioning in STM with a tenfold bandwidth, and a similar range of motion. The MEMS device features an integrated nanometer-sharp in-plane Si tip, compatible with conventional batch fabrication processes. In addition, a novel electrical isolation technique is developed to electrically isolate the tip from the rest of this device. This enables us to provide a separate routing for tunneling current signal, enabling potential applications in parallelism. The fabricated MEMS device achieves  $1.6\text{ }\mu\text{m}$  motion with its first in-plane resonance beyond  $10\text{ kHz}$ . The capability of this MEMS nanopositioner to replace the Z-axis of STMs is demonstrated through establishing controlled and stable tunneling current on a graphite sample in ambient conditions. [2020-0345]

**Index Terms**—Scanning tunneling microscopy, nanopositioner, integrated tip, oxide bridge, batch fabrication, feedback control loop.

## I. INTRODUCTION

SCANNING Tunneling Microscope (STM) is one of the most powerful and versatile tools in nanotechnology. The STM is commonly employed to obtain topographic images from a conductive surface at atomic levels [1], as well as to perform nanolithography, where a monolayer resist on a surface is patterned with atomic resolution [2]. Thanks to its ultra-high resolution and atomic precision, the STM has found use in single atom adsorption/desorption [3] and manipulation

applications [4]. All these features have contributed to the STM being recognized as a leading tool for fabrication of fascinating atomic-scale electronic devices, such as atomic wires [5], atomic-scale memories [6], atomic switches [7], atomic diodes [8], single molecule amplifiers [9], single-atom transistors [10], and solid state quantum computers [11]. Besides nanofabrication, the STM has been widely used for studying various characteristics of matter at the atomic scale [12], [13].

The working principle of STM relies on the electron tunneling from a nanometer-sharp tip to a conductive surface. The STM tip is usually mounted on a three Degree-of-Freedom (DOF) piezotube nanopositioner to position the tip close to the sample surface, e.g. about a nanometer or less. By applying an appropriate voltage bias between the tip and sample, electrons start tunnelling through the tip-sample gap [14]. The tunneling current value is exponentially proportional to the tip-sample distance, thus the atomic topography of the sample causes the tunneling current to vary during a scan [15]. Commonly, a control feedback loop is incorporated to maintain the tunneling current at a setpoint by keeping the tip-sample distance constant and regulating the Z-axis of the piezotube. STM images are constructed by plotting the controller output along the reference trajectories in the XY plane. The combination of the bias voltage, tunneling current setpoint, and electron dose values determines the STM mode for either imaging or lithography.

Despite its critical role in a variety of applications, conventional STM systems are not able to meet the requirements of the emerging applications in nanotechnology. STM is a fundamentally slow system, and its scan speed and throughput are limited for several reasons, like limited bandwidth of the piezotubes in the XY plane, underdamped dynamics of the piezotubes, and limited bandwidth of the current sensors. Another important limiting factor is the bandwidth of the piezotubes for Z-axis positioning, which determines how fast the piezotube can respond to changes in the sample topography during a scan. Since the piezotubes are bulky components, their Z-axis bandwidth is typically limited to about  $1\text{ kHz}$  with the tip assembly loaded [16], [17].

To address the bandwidth limitation issue, researchers have proposed flexure-guided [18]–[21] and dual-stage piezo-nanopositioners [22]. However, these technologies are yet to find their way into scanning tunneling microscopy. This is mainly due to their bulkiness and difficulties with their utilization in high-throughput nanofabrication applications [23].

Manuscript received October 11, 2020; revised December 14, 2020; accepted January 12, 2021. Date of publication January 26, 2021; date of current version March 16, 2021. This work was supported by the U.S. Department of Energy's Office of Energy Efficiency and Renewable Energy (EERE) through the Advanced Manufacturing Office under Award DEEE0008322. Subject Editor D. Elata. (Corresponding author: S. O. Reza Moheimani.)

Afshin Alipour and S. O. Reza Moheimani are with the Erik Jonsson School of Engineering and Computer Science, The University of Texas at Dallas, Richardson, TX 75080 USA (e-mail: afshin.alipour@utdallas.edu; reza.moheimani@utdallas.edu).

M. Bulut Coskun was with the Erik Jonsson School of Engineering and Computer Science, The University of Texas at Dallas, Richardson, TX 75080 USA. He is now with the Advanced Optical and Electromechanical Microsystems Group, NASA Jet Propulsion Laboratory, Pasadena, CA 91109 USA (e-mail: bulut.coskun@gmail.com).

Color versions of one or more figures in this article are available at <https://doi.org/10.1109/JMEMS.2021.3052180>.

Digital Object Identifier 10.1109/JMEMS.2021.3052180

1057-7157 © 2021 IEEE. Personal use is permitted, but republication/redistribution requires IEEE permission.

See <https://www.ieee.org/publications/rights/index.html> for more information.

In an attempt to fix issues arising from bulkiness and high-throughput utilization, flexure-guided nanopositioners have been miniaturized through microfabrication processes [24]–[28]. These devices offer large lateral bandwidths, a small footprint, and the potential for use in array configurations [29]. Despite such benefits, most of these devices suffer from slow Z-axis dynamics, ultimately limiting the scan speed.

In [30], we proposed a 1-DOF Microelectromechanical-Systems (MEMS) nanopositioner to replace the Z-axis of conventional STM piezo-nanopositioners. There, the design goal set for the MEMS device was to increase the Z-axis bandwidth of the STM system up to  $10\text{kHz}$ , while maintaining a Range of Motion (ROM) of approximately  $2\text{ }\mu\text{m}$ . In this work, we demonstrate a second-generation design that offers substantial improvements. First, we take advantage of anisotropic wet etching of doped Si to realize a sharp in-plane tip, which is suitable for batch production. This avoids the need for a post-fabrication process to deposit a Pt tip through Focus Ion Beam (FIB) deposition, which could be tedious, incompatible with batch fabrication processes, and requires skilled oversight. Moreover, we develop a novel electrical isolation technique using standard cleanroom tools to realize a moving shuttle beam comprised of sections that are electrically isolated, but mechanically connected. This allows us to separate the electrical routing for the tip and shuttle actuation within the device layer of an SOI wafer, in contrast to the double-SOI wafer approach demonstrated in our previous work [30].

The paper continues as follows. In the next section, we describe various design aspects of the MEMS device in detail. Then, in Section III we express the micromachining steps taken to fabricate the device. The static and dynamic behaviors of the fabricated device are subsequently assessed, and compared with the simulations in Section IV. Finally, we demonstrate the functionality of the device by conducting an experiment on a Highly Ordered Pyrolytic Graphite (HOPG) sample in ambient and report it in Section V.

## II. DEVICE COMPONENTS AND DESIGN PARAMETERS

A schematic overview of the device is illustrated in Fig. 1. The device is composed of a shuttle beam suspended by compliant flexures. An in-plane tip is fabricated at the end from which the device approaches the sample surface. An oxide bridge is implemented on the shuttle close to the tip, which electrically isolates the tip end of the shuttle from the rest of the device where the electrostatic actuators are located. The tensile and buckling strengths of the flexures prevent the beam from moving in the Y direction. In addition, the out-of-plane stiffness of the device along the X direction is designed to be higher than the in-plane stiffness along the Z direction to reduce mechanical vibrations. The actuators are also oriented towards Z direction. Other major aspects of the device are described in detail in the following subsections.

### A. Physical Dimensions

We ultimately aim to replace and improve the Z-axis positioning capabilities of an existing commercial STM by

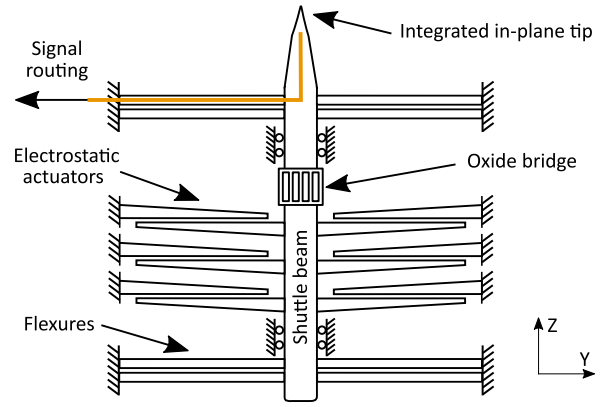


Fig. 1. Schematic of the MEMS device.

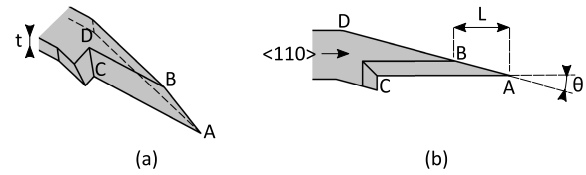


Fig. 2. Tip schematics: (a) isometric view (b) top view.

replacing the STM tip with this MEMS device. Therefore, the MEMS device should fit the area that the STM system permits. In a commercial STM of interest to us, the tip is mounted on a tip holder, made up of a gold plate with outer diameter of  $6\text{ mm}$ . This tip holder assembly is subsequently placed on a piezotube for tip positioning. In addition, the carrier on which the tip holder is transferred into Ultra-High-Vacuum (UHV) STM chamber, fits the tips with less than  $4.5\text{ mm}$  height. Thus, our MEMS device should not be wider than  $6\text{ mm}$  in Y direction and longer than  $4.5\text{ mm}$  in Z direction.

### B. STM Tip

A conductive tip is a critical component of any STM setup, since it enables direct interaction with the surface and is responsible for the electron tunneling. Therefore, the method selected for the tip fabrication is of great importance given that the tip is required to successfully perform imaging and lithography operations with the proposed device. Previously, we used a post-processing method based on FIB deposition [31], [32], to implement the tips on the microfabricated device [30]. While we have been able to obtain sharp functional tips with this method, its serial manner substantially prolongs the device fabrication process.

In contrast to our previous work, here we integrate the tips with the MEMS batch fabrication process by taking advantage of anisotropic wet etching of highly doped Si [33]. Figure 2 shows schematics of the in-plane tip. A Silicon-on-Insulator (SOI) wafer with crystallographic  $\langle 100 \rangle$  orientation is utilized to fabricate this tip. In this scheme, intersection of three planes forms a tip at point A: ABC plane is formed by wet etching of Si, ABD plane is formed by vertical dry etching of Si, and ACD plane is the bottom side of the device layer. Since the tip is made of Si, its conductivity depends on the doping

level of the wafer. The geometry of the tip can be adjusted by two parameters:  $t$  and  $\theta$ . The parameter  $t$  is the device layer thickness, and  $\theta$  is the angle at which the tip body deviates from the Si crystallographic  $\langle 110 \rangle$  direction, defined by photolithography process. The tip apex length,  $L$ , can be calculated as:

$$L = \frac{t}{\sqrt{2} \tan \theta}. \quad (1)$$

The angle of tip on the three aforementioned planes solely depends on  $\theta$ :  $\arctan(\sqrt{3} \tan \theta)$ ,  $\arctan(\sqrt{2} \sin \theta)$ , and  $\theta$ , respectively. The length and angles are important characteristics of this tip, but their effects on the tip geometry are opposing. As the tip angles become narrower, which is more favorable for scanning tunneling microscopy, the tip becomes longer. Longer tips are more susceptible to vibrations, deteriorating the STM performance. Therefore, a trade-off needs to be made while selecting  $\theta$  and  $t$ . In this work, we consider  $\theta = 15^\circ$  and  $t = 19 \mu\text{m}$ . The self-stopping nature of this tip fabrication method makes the overall microfabrication process conducive to mass production and allows us to obtain sharp tips throughout the wafer. The process flow for the tip fabrication is explained later in Section III. Inspecting the fabricated devices in one batch with Scanning Electron Microscope (SEM) revealed that apex radius of 90% of the fabricated tips was less than  $10 \text{ nm}$  on average, while the other 10% of the tips came out defective due to irregularities in the subsequent microfabrication steps.

### C. Electrical Isolation

In the MEMS implementation of the Z-axis STM nanopositioner, both the tip and the electrostatic actuators are parts of the shuttle beam. In order to enable the use of this device in an array configuration, it is necessary to isolate the electrical routings of the tip from the shuttle. To realize this, in our previous design we used a double-SOI wafer, where the top and bottom device layers were utilized to route out the tunneling current from the tip separate from the ground line going to the shuttle beam [30]. Here, the in-plane tip scheme requires the electrical isolation to be implemented in the same layer as the tip and shuttle beam. Therefore, the tip and the shuttle beam should be electrically isolated while remaining mechanically attached. To do this, we developed a method to fabricate a composite shuttle beam consisting of two Si bodies connected to each other by means of an oxide bridge.

The isolation method relies on the consumption of Si during wet thermal oxidation, and replacing the conductive slender Si beams bridging the shuttle sections with an insulator,  $\text{SiO}_2$ . The process starts with etching a set of five beams in the device layer, each  $2\text{-}\mu\text{m}$  wide and  $20\text{-}\mu\text{m}$  long. Then, these beams are thoroughly oxidized by wet oxidation in a furnace, which, in turn, consumes the whole Si in the bridge structure and increases the beam width to  $4.4 \mu\text{m}$ . In order to reinforce the beams, a  $0.8\text{-}\mu\text{m}$ -thick oxide layer is conformally deposited on the wafer with Low Pressure Chemical Vapor Deposition (LPCVD) technique, increasing the beam width to  $6 \mu\text{m}$ . For the Si device layer to be exposed again for subsequent steps, the oxide on the wafer surface is etched back. However,

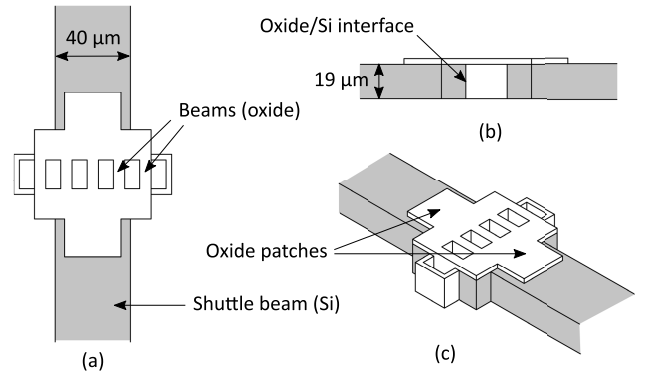


Fig. 3. Oxide bridge schematics: (a) top view (b) side view (c) isometric view.

we intentionally leave a patch of oxide at either side of the oxide bridge to further strengthen the oxide/Si interface. Figure 3 shows the schematics of the oxide bridge. The initial Si layer thickness is selected to be  $20 \mu\text{m}$ , reducing to  $19 \mu\text{m}$  after completion of the oxide bridge fabrication.

In general, implementation of this scheme on the shuttle beam requires optimizing the mechanical integrity of the beams to prevent the failure of the oxide bridge under force. Since the oxide is brittle material, flexures are put at both sides of the bridge structure, and actuators are implemented unidirectionally to ensure that the bridge region will be under compressive stress all the time. In addition, a preload compressing stress applied on the bridge when the tip is on the sample surface ensures that the inertia of the tip will not cause tensile stress in the bridge region during high-speed applications. Investigating the conductivity between the ground and tunneling current routings with an impedance analyzer (E4990A, Keysight Technologies) on the fabricated MEMS devices confirmed that the two sections of the shuttle beam were indeed electrically isolated. To the authors' knowledge, this is the first demonstration of a movable shuttle beam composed of two electrically separated sections capable of withstanding load and structural integrity.

### D. Actuation Methodology

Electrostatic parallel-plate actuation methodology is implemented in this device, as this transduction mechanism offers high resolution, fast response, and low creep over a few micrometers of range. The electrostatic force and input voltage (neglecting the fringing field effect) are related according to:

$$F_{es} = \frac{\epsilon A V^2}{2(d_0 - z)^2} = -k_z z, \quad (2)$$

where  $F_{es}$ ,  $\epsilon$ ,  $A$ ,  $V$ ,  $d_0$ ,  $k_z$ , and  $z$  are the electrostatic force, permittivity of the medium, total overlapping plate area, input voltage applied to the plates, initial gap, stiffness in Z direction, and displacement, respectively [34]. Of consideration is the effect of pull-in instability, which occurs when  $z$  is larger than one-third of  $d_0$ . To protect the device, we limit maximum value of  $z$  (stroke of the device) and  $d_0$ , to  $2 \mu\text{m}$  and  $7 \mu\text{m}$ , respectively. As a secondary precaution, a mechanical stopper



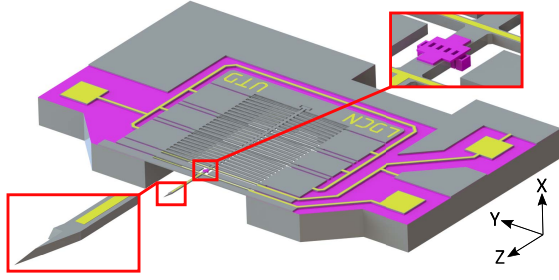


Fig. 4. CAD model of the MEMS device. The tip and oxide bridge are magnified in the close-up views.

is also implemented at the back-end of the shuttle beam to mechanically restrict large displacements.

#### E. Stiffness

The dynamic mode of a MEMS nanopositioner can be modeled as a second order spring-mass-damper system [35]–[37], where the cumulative stiffness of the suspension elements has a critical role both in device performance and functionality. Stiffness of the device along the Z-axis has to be sufficiently high to achieve bandwidth greater than  $10\text{ kHz}$ , and to be less susceptible to thermal noise and to avoid the snap-in effect arising from the intermolecular forces between the tip and sample during a scan [38]. In addition, the device needs to be compliant enough to reach the desired stroke (i.e.  $2\text{ }\mu\text{m}$ ) with a reasonable level of actuation voltage (i.e. less than  $100\text{ V}$  in a STM system).

Considering the aforementioned design criteria, a conservative estimate for the minimum required stiffness along the Z-axis was calculated as  $112\text{ Nm}^{-1}$  in our previous work [30]. Furthermore, thermal noise is a limiting factor for high-precision scanning probe microscopy, since it can excite mechanical resonances of the device. Due to the fact that MEMS devices are typically lightly damped, thermally excited resonances can deteriorate a system's performance. Based on the equipartition theorem, the thermal noise effect can be characterized by the following equation for a typical oscillator [39]:

$$\bar{x}_{th} = \sqrt{\frac{k_b T}{k}}, \quad (3)$$

where  $\bar{x}_{th}$  is the mean displacement induced by the thermal noise,  $k_b$  is the Boltzmann constant,  $T$  is temperature, and  $k$  is the stiffness along the desired direction. According to this equation, increasing the stiffness reduces thermally-induced vibrations. However, increased stiffness in Z direction leads to the requirement for a larger actuation force. Consequently, larger actuators become more prone to deflection, increasing the chance of electrical shorting. To address the requisite compromise, geometry of the double-clamped beam-type suspension elements are optimized through the Finite Element Analysis (FEA) simulations. In these simulations, the in-plane stiffness value along Z direction is designed to be as high as  $285\text{ Nm}^{-1}$ , while the out-of-plane stiffness of the device along X direction is obtained as  $505\text{ Nm}^{-1}$ .

TABLE I  
PROPERTIES OF THE MEMS DEVICE COMPONENTS

Feature type	Length ( $\mu\text{m}$ )	Width ( $\mu\text{m}$ )	Small base ( $\mu\text{m}$ )	Large base ( $\mu\text{m}$ )
Flexures	750	12	-	-
Flexures with routing	750	16	-	-
Actuator arm	730	-	10	30
Shuttle beam	2753	40	-	-
Tip	153	-	-	-

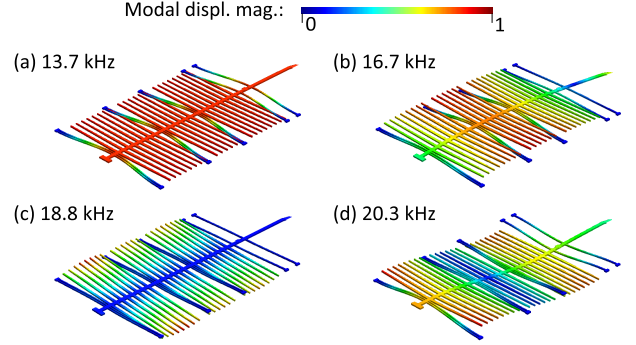


Fig. 5. Simulated mode shapes: (a) first, (b) second, (c) third, and (d) fourth mode.

#### F. Finite Element Simulations

The MEMS device is designed with CoventorWare software. Based on the design parameters discussed in the previous subsections, we built a Computer Aided Design (CAD) model of the device shown in Fig. 4. The overall dimensions of the device are  $4.3\text{ mm}$  in length and  $6\text{ mm}$  in width. The nan positioning device is  $19\text{ }\mu\text{m}$ -thick and comprises a  $2.7\text{ mm}$ -long shuttle beam with an in-plane tip, 16 slender flexures, and 44 pairs of parallel-plate electrostatic actuators. Table I summarizes the dimensions of the device components.

Since the nanopositioner is a distributed parameter system, its dynamic response is described by its natural frequencies and mode shapes. Hence, the modes shapes of the device are obtained using the FEA package, and shown in Fig 5. The first natural frequency of the device is  $13.7\text{ kHz}$  along the Z-axis, satisfying a key design criterion, while the remaining out-of-plane modes lie beyond  $16\text{ kHz}$ . It is noteworthy to mention that the oxide bridge has a negligible effect on the dynamics of the device. In a separate simulation where the model of the device was simplified by replacing the oxide bridge with the shuttle beam, the changes observed in the resonances were less than 1%, while the mode shapes stayed the same.

In parallel-plate electrostatic actuators, the pull-in phenomena limits the maximum allowable displacement of the device. For an ideal parallel-plate electrostatic actuator, the pull-in instability occurs at one-third of the initial gap. However, fringing field effect originating from the limited geometry of the actuators contributes to this instability. In order to have an accurate estimation of the pull-in voltage, the static response of the device under electrostatic actuation is simulated and illustrated in Fig. 6a. The result predicts that the shuttle beam displaces  $2.2\text{ }\mu\text{m}$  in Z direction just before the

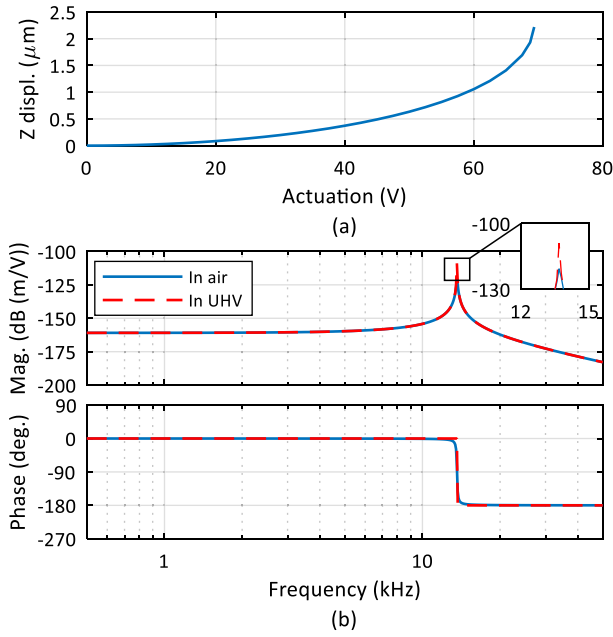


Fig. 6. Simulated displacement characteristics: (a) static response (b) frequency response.

pull-in instability occurs at 69.4 V, which is comparable to the required voltage for the same Z-motion in a common STM piezotube.

Finally, because the Z-axis of the device is equipped with actuators, the resonance of the system along this axis needs to be obtained under electrostatic actuation force. The superposition of a DC voltage, i.e. 20 V, and a small-amplitude AC signal is applied to the device actuators in various frequencies. Under assumption of squeezed film damping between actuator plates, the displacement response of the shuttle in Z direction is determined for each frequency and depicted in Fig. 6b. Simulations show that resonance happens at 13.6 kHz with 40.2 dB dynamic range, which is typical of lightly damped behavior of MEMS devices. The resonance frequency obtained here is lower than the device's first natural frequency. This could be attributed to two causes: the softening effect of the applied DC voltage, and velocity damping effect. Since the majority of the STM systems work in UHV conditions, it is necessary to assess the UHV effect on the underdamped behaviour of the MEMS device. We repeated the same simulation under UHV conditions with  $10^{-10}$  Torr pressure, and included the result in Fig. 6b. This simulation predicts that the dynamic range of the device will increase by 11.8 dB in UHV conditions.

### III. MICROFABRICATION

A highly doped SOI wafer (0.001-0.005  $\Omega\text{cm}$ , N-type,  $\langle 100 \rangle$ ) with a 20- $\mu\text{m}$  device layer, 2- $\mu\text{m}$  Buried Oxide (BOX) layer, and 400- $\mu\text{m}$  handle layer is chosen for the fabrication of the 1-DOF MEMS nanopositioner (Fig. 7a). The fabrication process starts with defining the bridge geometry by etching the device layer down to the BOX layer with the Deep Reactive Ion Etching (DRIE) process (Fig. 7b and Fig. 8a).

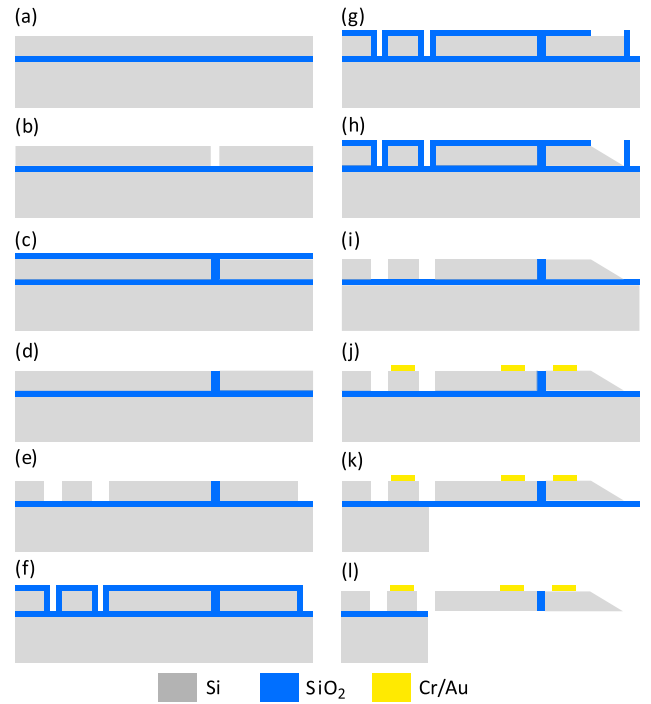


Fig. 7. Microfabrication flow: (a) initial SOI wafer (b) bridge body formation (c) thermal oxidation with subsequent LPCVD oxide deposition (d) RIE of the oxide (e) DRIE of the device layer (f) sacrificial oxide layer deposition (g) oxide openings formation with RIE (h) wet etching of Si (i) stripping the sacrificial oxide layer (j) electrode deposition (k) DRIE of the handle layer (l) releasing the device by RIE of the BOX layer.

Then, the wafer undergoes a wet thermal oxidation step at 1100°C to thoroughly oxidize the bridge (Fig. 8b). In order to reinforce the oxide bridge, a 0.8- $\mu\text{m}$  oxide layer is conformally deposited all over the wafer using LPCVD process (Fig. 7c). The oxide bridge fabrication is concluded by etching back the oxide on the device layer by Reactive Ion Etching (RIE) process to expose the Si layer again for the subsequent steps (Fig. 7d and Fig. 8c).

All other components of the MEMS nanopositioner, such as shuttle beam, actuators, flexures, and bonding pads are formed at the same time by patterning and etching the device layer with DRIE process (Fig. 7e and Fig. 8d). It is during this step that the tip body is also formed with the angle of  $\theta = 15^\circ$  with respect to the Si crystallographic  $\langle 110 \rangle$  plane (Fig. 8e). Then, a sacrificial 300-nm oxide layer is deposited with LPCVD process to conformally cover the tip body (Fig. 7f). Afterwards, a window in the oxide layer is opened on top of the tip body with RIE process to define a mask for Si wet etch (Fig. 7g and Fig. 8f). Thanks to the sacrificial oxide layer, only the tip body is then anisotropically etched away in a 45% KOH solution to form the tip (Fig. 7h and Fig. 8g). The tip formation is concluded by etching away the sacrificial oxide layer with buffered oxide etch solution (Fig. 7i and Fig. 8h).

In order to provide signal routing and bonding pads, a stack of 20-nm Cr and 280-nm Au layers are sputtered and patterned on the device features with a lift-off process (Fig. 7j). At the last steps of the fabrication, the handle layer is patterned and

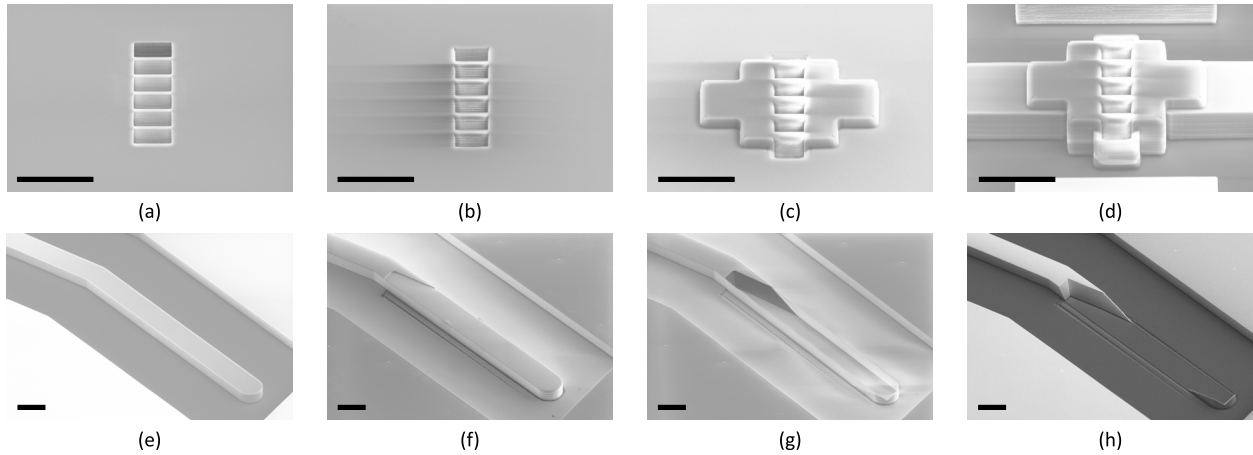


Fig. 8. SEM images of the device at different stages of fabrication: (a) beams (b) oxidizing the beams (c) exposing the Si device layer (d) DRIE of the device layer (e) tip body (f) sacrificial LPCVD oxide defined as a wet etch mask (g) in-plane tip (h) stripping the sacrificial oxide layer. All scale bars are  $40\ \mu\text{m}$ .

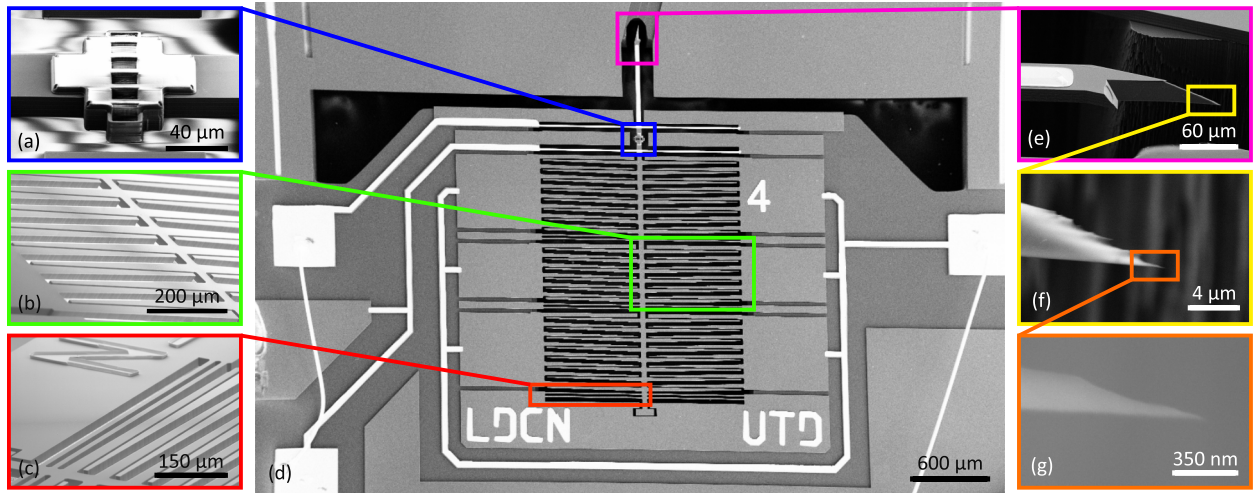


Fig. 9. SEM images of the fabricated device: (a) oxide bridge (b) parallel-plate electrostatic actuators (c) compliant flexures (d) MEMS device (e) tip shank (f) in-plane Si tip (g) tip apex.

etched up to the BOX layer from the back side with DRIE process (Fig. 7k). Then, RIE process is used to etch away the BOX layer and release the nanopositioner (Fig. 7l). Figure 9 shows the SEM images of the fabricated nanopositioner.

#### IV. CHARACTERIZATION

Important characteristics of the fabricated MEMS nanopositioner are empirically measured here in order to extract necessary parameters for the experiments. These properties include maximum achievable displacement, transfer function estimate for the first mode dynamics, mode shapes of the device, and feedthrough capacitance.

##### A. Static Response

The actuation voltage-displacement trend of the device is experimentally observed to determine the required voltage levels for the desired stroke. During the experiments, a  $4\text{-Hz}$  triangular signal is applied to the electrostatic actuators using a function generator cascaded with a voltage amplifier. Then,

the displacement trend for the corresponding actuation voltage is simultaneously monitored using a Polytec MSA-100-3D Laser Doppler Vibrometer (LDV). The measurements are plotted in Fig. 10a. Results show that the shuttle beam displaces  $1.6\ \mu\text{m}$  when the actuation voltage is  $70.2\ \text{V}$ . The discrepancy between predicted and measured displacements is due to the microfabrication tolerances and measurement errors.

##### B. Frequency Response

Frequency response of the device from the input voltage (with  $20\text{-V}$  DC offset) to the tip displacement is obtained by the LDV in ambient conditions and reported in Fig. 10b. Results show that the first resonant frequency of the device is located at  $10.7\ \text{kHz}$ . The lower resonance obtained empirically is due to microfabrication tolerances and the fact that the simulation did not allow for other sources of damping, such as internal damping of the material. A second-order model with the following transfer function is fitted to the frequency response of the device in Fig. 10b to characterize the first mode



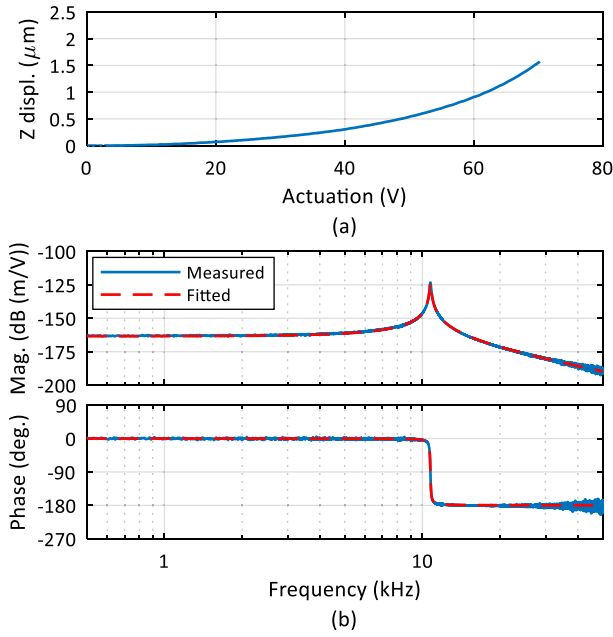


Fig. 10. Measured displacement characteristics: (a) static response (b) frequency response.

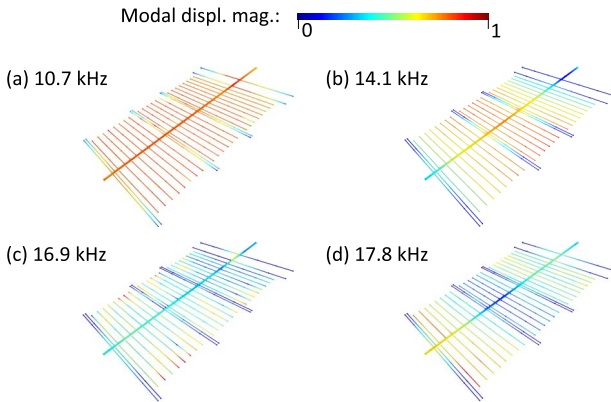


Fig. 11. Measured mode shapes: (a) first, (b) second, (c) third, and (d) fourth mode.

dynamic response of the system:

$$G_m(s) = \frac{30.58}{s^2 + 655.4s + 4.552 \times 10^9}. \quad (4)$$

### C. Mode Shapes

Figure 11 illustrates the first four mode shapes of the device in ambient conditions. During this experiment, the surface of the nanopositioner is scanned through the predefined points using the LDV, and the frequency response of the nanopositioner is obtained at each point in order to construct the mode shapes. The experimental mode shapes in Fig. 11 are in good agreement with the predicted ones reported in Fig. 5. Moreover, the slight discrepancy in the predicted and measured values of the resonant frequencies can be attributed to the microfabrication tolerances.

### D. Feedthrough Capacitance

Electrical cross-coupling between actuation and sensing signals is a common phenomenon in MEMS devices, arising from closely spaced electrical routings on the same substrate. The substrate can act as a medium to superimpose the actuation signal on the sensor output. This undesired effect, also known as electrical feedthrough, exhibits a high-pass characteristics and can be modeled as a capacitor between the actuation and sensing terminals [31]. As the tunneling current amplitude in STM applications is quite small, the feedthrough signal can corrupt the tunneling current measurements. Hence, this effect needs to be investigated prior to the experiment.

Using the experimental equipment described in Section V, we assessed the feedthrough capacitance in the fabricated devices with a lock-in technique. Experiments show that the parasitic feedthrough capacitance is less than  $0.01 \text{ pF}$ . We expect no adverse effect on the tunneling current measurements arising from the feedthrough effect in this device.

## V. EXPERIMENTS

In this section, the capabilities of the proposed MEMS device in STM experiments is demonstrated by establishing and maintaining a stable tunneling current on an HOPG sample at ambient conditions.

### A. Experimental Setup

In order to achieve mechanical stability and vertical sample positioning, we employed the motorized stage of an existing Atomic Force Microscope setup (AFM) (TT-AFM, AFM-Workshop) in our experimental platform (Fig. 12). The original AFM piezo-scanner is replaced with a 3-DOF piezopositioner (P-363.3CD, Physik Instrumente), which provides finer positioning in 3D. The MEMS device is mounted on and wirebonded to a custom Printed Circuit Board (PCB) to interface the device with the driver and read-out electronics. Next, the PCB is bolted vertically on the piezopositioner using a custom design adapter, whereas the HOPG sample is magnetically clamped upside down to the motorized stage as shown in the close-up view in Fig. 12. The complete experimental platform is kept inside an enclosure, whose interior is covered by Al foil for electromagnetic shielding. The cabinet is placed on an optical table to minimize external vibrations, and the cabinet door is kept closed to reduce disturbances during the experiments.

The motorized AFM stage and the piezopositioner work synchronously in the Z-axis to automatically bring the sample and the MEMS close to each other such that the sample gets within the ROM of the MEMS. Here, the piezopositioner is driven by a piezo-controller (E-536.3CH, Physik Instrumente) in closed-loop mode to minimize nonlinearities such as hysteresis, creep, and drift during the coarse-positioning. A rapid control prototyping unit (MicroLabBox, dSpace) running at  $50\text{-kHz}$  sampling frequency is utilized to implement algorithms required for coarse positioning, establishing the tunneling current with the MEMS device, and monitoring. Other equipment used in the experiments includes a voltage amplifier (A400DI, FLC Electronics) with fixed gain of 20 to

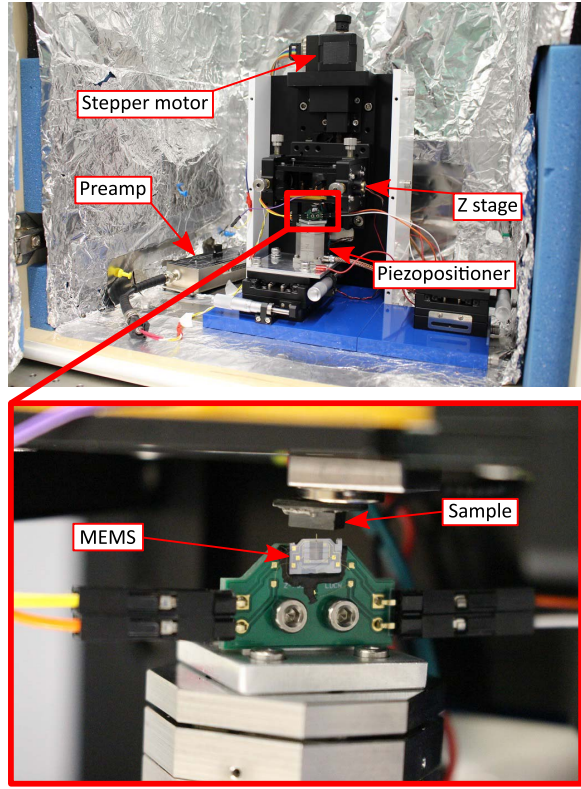


Fig. 12. Experimental setup.

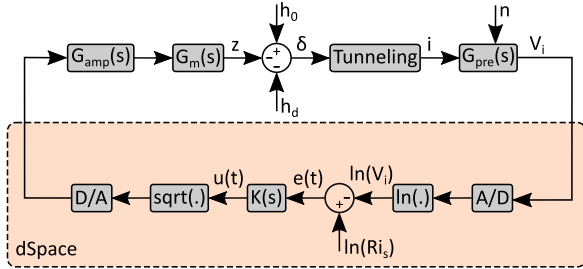


Fig. 13. Block diagram of the closed-loop system.

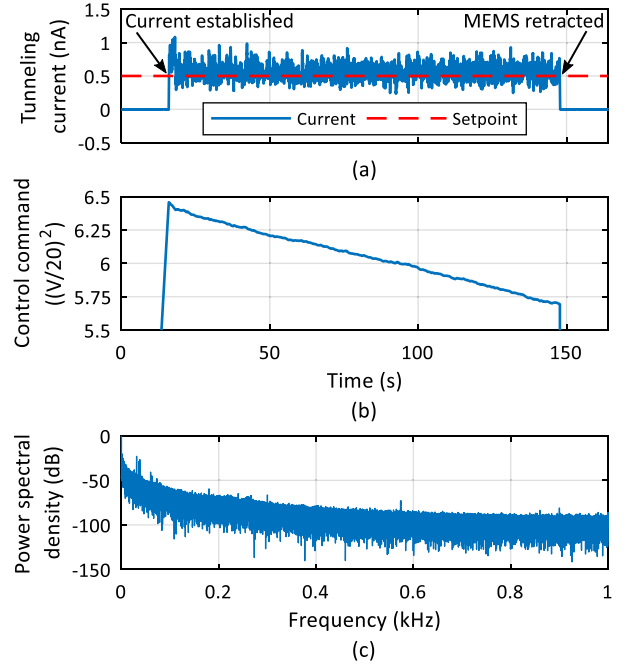
provide required actuation voltage for the MEMS device, and a variable gain low noise current preamplifier (DLPCA-200, Femto) to convert the tunneling current signal to a measurable voltage signal.

### B. Closed-Loop Structure

After the tunneling current is established, a feedback loop regulates the MEMS to maintain the tunneling current at a setpoint. Figure 13 illustrates a simplified block diagram detailing the feedback loop structure. The voltage amplifier,  $G_{amp}(s)$ , provides the required voltage for driving the MEMS nanopositioner,  $G_m(s)$ , changing the tip-sample gap,  $\delta$ , which is approximately equal to the barrier thickness:

$$\delta = h_0 - h_d - z, \quad (5)$$

where  $h_0$  is the initial distance between the MEMS tip and sample, and  $h_d$  accounts for the disturbances, e.g. drift. Here

Fig. 14. Experimental results: (a) tunneling current signal (b) control command ( $u(t)$ ) (c) power spectral density of the tunneling current signal.

$\delta$  translates into a current, as follows [15]:

$$i = \sigma V_b e^{-1.025\sqrt{\phi}\delta}. \quad (6)$$

In this equation,  $\sigma$  is a constant term that depends on the material properties of the tip and sample, whereas  $V_b$  and  $\phi$  are the sample bias and barrier height, respectively. The preamplifier ( $G_{pre}(s)$ ) converts the nano-ampere level current into a measurable voltage,  $V_i$ . In order to minimize the measurement noise ( $n$ ), the bandwidth and gain ( $R$ ) of the preamplifier are set to 10 Hz and 1 V/nA, respectively. The  $V_i$  signal is discretized by one of the Analog-to-Digital (A/D) converters available in dSpace to be used in the control loop. As pointed out by Eq. 6, tunneling current is an exponential function of the tip-sample gap, and likewise of the MEMS motion. Therefore, it is necessary to take the natural logarithm of the signal to provide a linear dependency, as follows:

$$\ln(Ri) = \ln(R\sigma V_b) - 1.025\sqrt{\phi}\delta. \quad (7)$$

Here,  $\ln(V_i)$  is compared with logarithm of the setpoint, and the resulting error signal is fed into the controller,  $K(s)$ . Although the error signal is discrete, the control scheme can be described in continuous time domain due to the high sampling frequency. The controller here is considered to be an integrator with the following equation:

$$K(s) = \frac{K_i}{s}, \quad (8)$$

where the integrator gain  $K_i$  is set to 0.2, based on which the controller command,  $u(t)$ , is determined. The square root of this signal is then taken to eliminate the quadratic dependency of  $z$  displacement on the applied voltage, as pointed out in Eq. 2. Finally, a Digital-to-Analog (D/A) converter in dSpace



converts the resulting discrete signal into an analog one to be used by the amplifier.

### C. Experimental Results

For the experiments, the current setpoint and sample bias are set to  $0.5\text{ nA}$  and  $-1\text{ V}$ , respectively. After the coarse motion mechanism brings the sample within the ROM of the MEMS, the MEMS approaches the sample surface during the first  $16\text{ s}$  and establishes the tunneling current. During the experiments, we were able to successfully establish and maintain a stable tunneling current on the HOPG sample in the ambient conditions several times without crashing the tip into the surface. A typical result is depicted in Fig 14. Here, the controller maintains the tunneling current at the setpoint for more than two minutes by rejecting the disturbances until the MEMS was retracted (Fig 14 a). Inspecting the controller command in Fig 14 b, however, reveals the existence of a drift in the setup, which was successfully canceled by the feedback-loop. The root-mean-square value of the error between the current and its setpoint is calculated as  $0.107\text{ nA}$ , which is mostly due to the drift.

## VI. CONCLUSION

In this work, we presented the design, fabrication, and characterization of a new 1-DOF MEMS nanopositioner to replace the Z-axis of the conventional STM piezotubes and the STM tip. The device incorporates an integrated in-plane Si tip suitable for batch fabrication processes. In order to enable parallelism, a novel electrical isolation scheme is proposed and implemented to electrically isolate the tunneling signal. This allows current sensors to be put at the tip side. By integrating the device into the currently available STM systems, the Z-axis bandwidth can be increased beyond  $10\text{ kHz}$ , while retaining the same ROM. The functionality of the device was demonstrated by conducting experiments on an HOPG sample in ambient conditions.

Our approach offers a unique opportunity for parallelism in STM through the design of an integrated tip and a novel electrical isolation scheme. This ensures the uniformity of the STM tips throughout the wafer. Future efforts will involve proposing an array of 1-DOF MEMS STM nanopositioners based on these schemes to further improve the throughput of the STM systems, and demonstrating imaging and lithography with the proposed device in UHV.

## ACKNOWLEDGMENT AND DISCLAIMER

### Acknowledgment

Facilities provided by The University of Texas at Dallas Cleanroom Research Laboratory were used to fabricate this device.

### Disclaimer

This manuscript was prepared as an account of work sponsored by an agency of the United States Government. Neither the United States Government nor any agency thereof, nor any of their employees, makes any warranty,

express or implied, or assumes any legal liability or responsibility for the accuracy, completeness, or usefulness of any information, apparatus, product, or process disclosed, or represents that its use would not infringe privately owned rights. Reference herein to any specific commercial product, process, or service by trade name, trademark, manufacturer, or otherwise does not necessarily constitute or imply its endorsement, recommendation, or favoring by the United States Government or any agency thereof. The views and opinions of authors expressed herein do not necessarily state or reflect those of the United States Government or any agency thereof.

## REFERENCES

- [1] G. Binnig and H. Rohrer, "Scanning tunneling microscopy," *Surf. Sci.*, vol. 126, nos. 1–3, pp. 236–244, 1983.
- [2] J. N. Randall, J. H. G. Owen, J. Lake, and E. Fuchs, "Next generation of extreme-resolution electron beam lithography," *J. Vac. Sci. Technol. B, Nanotechnol. Microelectron., Mater., Process., Meas., Phenomena*, vol. 37, no. 6, Nov. 2019, Art. no. 061605.
- [3] T. R. Huff *et al.*, "Atomic white-out: Enabling atomic circuitry through mechanically induced bonding of single hydrogen atoms to a silicon surface," *ACS Nano*, vol. 11, no. 9, pp. 8636–8642, Sep. 2017.
- [4] D. M. Eigler and E. K. Schweizer, "Positioning single atoms with a scanning tunnelling microscope," *Nature*, vol. 344, no. 6266, pp. 524–526, Apr. 1990.
- [5] L. Soukiassian, A. J. Mayne, M. Carbone, and G. Dujardin, "Atomic wire fabrication by STM induced hydrogen desorption," *Surf. Sci.*, vol. 528, nos. 1–3, pp. 121–126, Mar. 2003.
- [6] F. E. Kalf *et al.*, "A kilobyte rewritable atomic memory," *Nature Nanotechnol.*, vol. 11, no. 11, pp. 926–929, Nov. 2016.
- [7] D. M. Eigler, C. P. Lutz, and W. E. Rudge, "An atomic switch realized with the scanning tunnelling microscope," *Nature*, vol. 352, no. 6336, pp. 600–603, Aug. 1991.
- [8] I.-W. Lyo and P. Avouris, "Negative differential resistance on the atomic scale: Implications for atomic scale devices," *Science*, vol. 245, no. 4924, pp. 1369–1371, Sep. 1989.
- [9] C. Joachim and J. K. Gimzewski, "An electromechanical amplifier using a single molecule," *Chem. Phys. Lett.*, vol. 265, nos. 3–5, pp. 353–357, Feb. 1997.
- [10] M. Fuechsle *et al.*, "A single-atom transistor," *Nature Nanotechnol.*, vol. 7, no. 4, pp. 242–246, Feb. 2012.
- [11] M. Y. Simmons *et al.*, "Towards the atomic-scale fabrication of a silicon-based solid state quantum computer," *Surf. Sci.*, vols. 532–535, pp. 1209–1218, Jun. 2003.
- [12] K. M. Horn, B. S. Swartzentruber, G. C. Osbourn, A. Bouchard, and J. W. Bartholomew, "Electronic structure classifications using scanning tunneling microscopy conductance imaging," *J. Appl. Phys.*, vol. 84, no. 5, pp. 2487–2496, Sep. 1998.
- [13] S. Fölsch, P. Hyldgaard, R. Koch, and K. H. Ploog, "Quantum confinement in monatomic Cu chains on Cu(111)," *Phys. Rev. Lett.*, vol. 92, no. 5, Feb. 2004, Art. no. 056803.
- [14] G. Binnig, H. Rohrer, C. Gerber, and E. Weibel, "Tunneling through a controllable vacuum gap," *Appl. Phys. Lett.*, vol. 40, no. 2, pp. 178–180, Jan. 1982.
- [15] N. Lang, "Apparent barrier height in scanning tunneling microscopy," *Phys. Rev. B, Condens. Matter*, vol. 37, no. 17, p. 10395, 1988.
- [16] F. Tajaddodianfar, S. O. R. Moheimani, and J. N. Randall, "Scanning tunneling microscope control: A self-tuning PI controller based on online local barrier height estimation," *IEEE Trans. Control Syst. Technol.*, vol. 27, no. 5, pp. 2004–2015, Sep. 2019.
- [17] F. Tajaddodianfar, S. O. R. Moheimani, J. Owen, and J. N. Randall, "On the effect of local barrier height in scanning tunneling microscopy: Measurement methods and control implications," *Rev. Sci. Instrum.*, vol. 89, no. 1, 2018, Art. no. 013701.
- [18] G. Schitter, K. J. Astrom, B. E. DeMartini, P. J. Thurner, K. L. Turner, and P. K. Hansma, "Design and modeling of a high-speed AFM-scanner," *IEEE Trans. Control Syst. Technol.*, vol. 15, no. 5, pp. 906–915, Sep. 2007.
- [19] T. Ando *et al.*, "High-speed atomic force microscopy for capturing dynamic behavior of protein molecules at work," presented at the Int. Symp. Surf. Sci. Nanotechnol. (ISSS-4), Saitama, Japan, Dec. 2005.

- [20] Y. K. Yong and S. O. R. Mohemani, "Design of an inertially counterbalanced Z-nanopositioner for high-speed atomic force microscopy," *IEEE Trans. Nanotechnol.*, vol. 12, no. 2, pp. 137–145, Mar. 2013.
- [21] S. P. Wadikhaye, Y. K. Yong, and S. O. R. Mohemani, "A serial-kinematic nanopositioner for high-speed atomic force microscopy," *Rev. Sci. Instrum.*, vol. 85, no. 10, Oct. 2014, Art. no. 105104.
- [22] A. J. Fleming, "Dual-stage vertical feedback for high-speed scanning probe microscopy," *IEEE Trans. Control Syst. Technol.*, vol. 19, no. 1, pp. 156–165, Jan. 2011.
- [23] J. N. Randall *et al.*, "Highly parallel scanning tunneling microscope based hydrogen depassivation lithography," *J. Vac. Sci. Technol. B, Nanotechnol. Microelectron., Mater., Process., Meas., Phenomena*, vol. 36, no. 6, 2018, Art. no. 06JL05.
- [24] S. Akamine, T. R. Albrecht, M. J. Zdeblick, and C. F. Quate, "Micro-fabricated scanning tunneling microscope," *IEEE Electron Device Lett.*, vol. 10, no. 11, pp. 490–492, Nov. 1989.
- [25] Y. Xu, N. MacDonald, and S. Miller, "Integrated micro-scanning tunneling microscope," *Appl. Phys. Lett.*, vol. 67, no. 16, pp. 2305–2307, 1995.
- [26] M. Mita, H. Kawara, H. Toshiyoshi, J. Endo, and H. Fujita, "Bulk micromachined tunneling tips integrated with positioning actuators," *J. Microelectromech. Syst.*, vol. 14, no. 1, pp. 23–28, Feb. 2005.
- [27] E. Disseldorp *et al.*, "MEMS-based high speed scanning probe microscopy," *Rev. Sci. Instrum.*, vol. 81, no. 4, 2010, Art. no. 043702.
- [28] Y. Tang, Y. Zhang, G. K. Fedder, and L. R. Carley, "A dual probe STM imaging system and a low noise switched-capacitor transimpedance amplifier," *IEEE Sensors J.*, vol. 13, no. 8, pp. 2984–2992, Aug. 2013.
- [29] M. B. Coskun, M. Baan, A. Alipour, and S. O. R. Mohemani, "Design, fabrication, and characterization of a piezoelectric AFM cantilever array," in *Proc. IEEE Conf. Control Technol. Appl. (CCTA)*, Aug. 2019, pp. 227–232. [Online]. Available: <https://ieeexplore.ieee.org/abstract/document/8920686>
- [30] A. Alipour, M. B. Coskun, and S. O. R. Mohemani, "A high bandwidth microelectromechanical system-based nanopositioner for scanning tunneling microscopy," *Rev. Sci. Instrum.*, vol. 90, no. 7, Jul. 2019, Art. no. 073706.
- [31] M. B. Coskun, A. G. Fowler, M. Maroufi, and S. O. R. Mohemani, "On-chip feedthrough cancellation methods for microfabricated AFM cantilevers with integrated piezoelectric transducers," *J. Microelectromech. Syst.*, vol. 26, no. 6, pp. 1287–1297, Dec. 2017.
- [32] M. B. Coskun, H. Alemansour, A. G. Fowler, M. Maroufi, and S. O. R. Mohemani, " $Q$  control of an active AFM cantilever with differential sensing configuration," *IEEE Trans. Control Syst. Technol.*, vol. 27, no. 5, pp. 2271–2278, Sep. 2018.
- [33] R. P. Ried, H. J. Mamin, B. D. Terris, L.-S. Fan, and D. Rugar, "6-MHz 2-N/m piezoresistive atomic-force microscope cantilevers with INCISIVE tips," *J. Microelectromech. Syst.*, vol. 6, no. 4, pp. 294–302, 1997.
- [34] S. D. Senturia, *Microsystem Design*. Berlin, Germany: Springer, 2007.
- [35] S. I. Moore, M. B. Coskun, T. Alan, A. Neild, and S. O. R. Mohemani, "Feedback-controlled MEMS force sensor for characterization of micro-cantilevers," *J. Microelectromech. Syst.*, vol. 24, no. 4, pp. 1092–1101, Aug. 2015.
- [36] M. B. Coskun, S. Moore, S. O. R. Mohemani, A. Neild, and T. Alan, "Zero displacement microelectromechanical force sensor using feedback control," *Appl. Phys. Lett.*, vol. 104, no. 15, Apr. 2014, Art. no. 153502.
- [37] M. Maroufi, H. Alemansour, M. B. Coskun, and S. O. R. Mohemani, "An adjustable-stiffness MEMS force sensor: Design, characterization, and control," *Mechatronics*, vol. 56, pp. 198–210, Dec. 2018.
- [38] A. Alipour, M. M. Zand, and H. Daneshpajooh, "Analytical solution to nonlinear behavior of electrostatically actuated nanobeams incorporating van der Waals and Casimir forces," *Scientia Iranica. Trans. F, Nanotechnol.*, vol. 22, no. 3, p. 1322, 2015.
- [39] P. R. Saulson, "Thermal noise in mechanical experiments," *Phys. Rev. D, Part. Fields*, vol. 42, no. 8, p. 2437, 1990.



**Afshin Alipour** received the B.Sc. degree in mechanical engineering from the Amirkabir University of Technology, Iran, in 2013, and the M.Sc. degree in applied mechanics from the University of Tehran, Iran, in 2016. He is currently pursuing the Ph.D. degree with the Department of Mechanical Engineering, The University of Texas at Dallas, USA. His research interests include high-precision mechatronics, control engineering, microsystems, microfabrication, and dynamics.



**M. Bulut Coskun** received the B.Sc. and M.Sc. degrees in mechatronics engineering from Sabanci University, Istanbul, Turkey, in 2009 and 2011, respectively, and the Ph.D. degree in mechanical and aerospace engineering from Monash University, VIC, Australia, in 2015. Later on, he joined The University of Texas at Dallas, as a Research Associate, where he developed active microcantilevers, cantilever arrays, and MEMS nanopositioners for high-speed and high-throughput scanning probe microscopy applications. In 2019, he joined

the NASA Jet Propulsion Laboratory (JPL), as a Post-Doctoral Researcher. His current research activities at JPL include design, FEA, nanofabrication, and characterization of MEMS transducers and SAW devices for the Advanced Optical and Electromechanical Microsystems Group.



**S. O. Reza Mohemani** (Fellow, IEEE) received the B.Sc. degree in electrical engineering from Shiraz University, Iran, in 1990, and the M.Eng.Sc. and Ph.D. degrees in electrical engineering from the University of New South Wales, Australia, in 1993 and 1996, respectively.

He holds the James Von Ehr Distinguished Chair in Science and Technology with the Department of Systems Engineering, The University of Texas at Dallas, with appointments in the Electrical and Computer Engineering and Mechanical Engineering departments. He is also the Founding Director of the UTD Center for Atomically Precise Fabrication of Solid-State Quantum Devices and the Founder and Director of the Laboratory for Dynamics and Control of Nanosystems. His current research interests include the applications of control and estimation in high-precision mechatronic systems, high-speed scanning probe microscopy, and atomically precise manufacturing. He is leading a multidisciplinary effort to develop new tools and methods for fabrication of solid-state quantum devices with atomic precision based on ultra-high vacuum scanning tunneling microscope. He is a Fellow of IFAC and the Institute of Physics (U.K.). He received the Charles Stark Draper Innovative Practice Award (ASME DSCD) in 2020, the Nathaniel B. Nichols Medal (IFAC) in 2014, the IEEE Control Systems Technology Award (IEEE CSS) in 2009, and the IEEE TRANSACTIONS ON CONTROL SYSTEMS TECHNOLOGY Outstanding Paper Award (IEEE CSS) in 2007 and 2018. He is the Editor-in-Chief of *Mechatronics*, and a past Associate Editor of IEEE TRANSACTIONS ON CONTROL SYSTEMS TECHNOLOGY, IEEE/ASME TRANSACTIONS ON MECHATRONICS and *Control Engineering Practice*.